

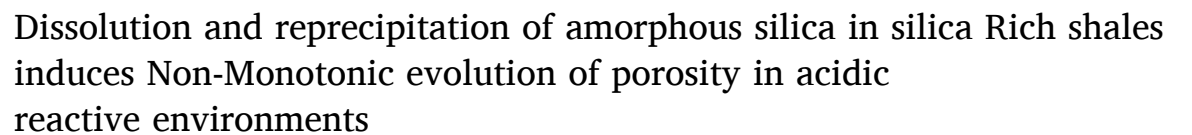
Contents lists available at ScienceDirect

Fuel

journal homepage: www.elsevier.com/locate/fuel



Full Length Article





Hassnain Asgar ^a, Sohaib Mohammed ^a, Alexa Socianu ^b, John Kaszuba ^b, Pavel D. Shevchenko ^c, Greeshma Gadikota ^{a,*}

- ^a School of Civil and Environmental Engineering, Cornell University, Ithaca, NY 14853, USA
- ^b Department of Geology and Geophysics, University of Wyoming, Laramie, WY 82071, USA
- ^c X-ray Science Division, Advanced Photon Source, Argonne National Laboratory, Lemont, IL 60439, USA

ARTICLE INFO

Keywords:
Shale
Porosity
Mineralogy
Amorphous and crystalline silica
X-ray scattering
X-ray microtomography

ABSTRACT

Advances in sustainable subsurface energy technologies are crucial for meeting our energy and resource needs for a climate-resilient future. Novel strategies to harness subsurface shale reservoirs for recovering valuable metals and for enabling CO₂ storage are influenced by the morphological and mineralogical heterogeneities of these materials. In this context, delineating the interactions of highly acidic solutions such as wet supercritical CO2 on shales with varying mineralogy is crucial to inform the stability of caprock seal for CO2 storage and enhancements in permeability for fluid transport, reactivity, and storage. The feedback chemical effects associated with the interactions of acidic solutions on the morphologies and mineralogies of shales have not been extensively investigated. These insights are crucial for assessing temporal changes in the reactivity and the fate of the fluids in subsurface environments. In this study, we investigate the effect of 1 M HCl solution on the chemistry and morphology of three different shale samples with varying carbonate, clay and silica contents. An increase in the amorphous content, from 37 % to 41.3 %, of silica-rich and carbonate/clay lean shale is noted due to reactions with an acidic solution which is attributed to the dissolution of Si-bearing phases such as clays, accompanied by SiO₂ precipitation. In shales bearing high content of clays and carbonates, significant increase in the pore volumes and surface areas are noted. Non-monotonic changes in the micron-scale porosity of silica rich – carbonate/ clay lean (e.g., Mowry shale) are noted using in-situ X-ray microtomography experiments. Due to the initial mobilization of silica and dissolution of carbonate/clay phases, the total porosity slightly increases from 6.7 % to 10.7 % followed by a decrease to ~4 % caused by SiO₂ reprecipitation. These findings suggest that even though silica is less reactive in acidic environments, the changes in the amorphous and crystalline content due to dissolution and reprecipitation alter the porosity and fluid flow paths.

1. Introduction

The dual needs to sustainably meet our growing energy and resource demand and limit detrimental impacts on climate and the environment motivate advances in transformative subsurface energy technologies including CO₂ storage in unconventional reservoirs [1–5]. As with engineered carbon storage via carbon mineralization [1,4,14–16,6–13], it is essential to consider the feedback effects of reactivity on the mineralogical and morphological changes of the underlying substrates. Unanticipated changes in the pore morphology and permeability impact

long-term projections of fluid storage (e.g., CO_2) in these environments. While CO_2 storage in siliceous environments (e.g., sandstone with permeability in the range of 0.01 to 100 mD) has been extensively investigated [17–21], there is a limited scientific understanding of the fate and transport of CO_2 in nano-porous shales with permeability in the range of 0.1 μ D–0.009 mD [21,22]. Furthermore, in supercritical CO_2 -rich and water lean environments, this fluid mixture is known to act as a super acid and rapidly dissolve basic minerals [23,24]. This highly reactive behavior has significant implications for the stability of shale as a stable overburden impermeable layer that prevents the migration of

E-mail address: gg464@cornell.edu (G. Gadikota).

 $^{^{\}ast}$ Corresponding author.

 ${\rm CO}_2$ to the surface [25]. Alternatively, there is interest in storing ${\rm CO}_2$ directly in shales in which case the influence of highly acidic environments such as those created by wet supercritical ${\rm CO}_2$ need to be resolved [26]. With more than 60 % of current oil and gas production coming from shales (e.g., unconventional hydrocarbon reservoirs) [27], these depleted reservoirs offer tremendous potential for subsurface ${\rm CO}_2$ storage [7,28–30]. Furthermore, the recovery of useful metals such as vanadium from shales typically requires acid-based leaching [31–33]. The key scientific uncertainty underlying these diverse applications is the mineralogical and morphological transformation of shales in acidic environments.

Shales comprise siliceous phases such as silica (predominantly as quartz), carbonaceous phases such as calcite, and clay-bearing phases such as illite. Calcite and clays readily dissolve in acidic solutions, while silica dissolution occurs at elevated pH environments. The mineralogy and morphology resulting from acid-induced dissolution influence subsequent fluid access, transport, and reactivity into these environments. While it is expected that the varying mineralogies of shales influence their reactivity with acidic solutions [34,35], the resulting morphological changes as a function of the composition of shales (especially for silica content) remain unresolved. Furthermore, the influence of the mobilization of fine particles resulting from the acid-induced treatment of shales on the resulting porosity of shales needs to be resolved.

Prior insights into the influence of acidic solutions on the mineralogies and morphologies of shales are important to evaluate in this context. Hydraulic fracturing is normally used to access oil and gas buried deep in these shales [36]. However, for shales around the depth of 3,000 m–4,000 m, the hydraulic fracturing approach can result in

safety issues due to the high breakdown pressures required at such depths. To circumvent this challenge of requiring high pressures, acid fracturing (acidizing) is sometimes applied as an alternative or pre-step to alter the properties of reservoir rocks and increase the permeability of the reservoirs [34,35,37,38]. Acidizing dissolves various mineralogical phases in shales and creates flow channels to assist with the flow of hydrocarbons. Acidizing is known to enhance the conductivity of natural microfractures [35,39] by dissolving the carbonate content. However, the influence of acids on the underlying siliceous structure remains unresolved. Prior studies investigating the influence of acids on the solubility of various magnesium silicate structures showed that dehydroxylated siliceous structures are more soluble compared to highly crystalline phases [40]. The bonding between Si and O in silicate species is determined using the number of bridging oxygens (BO) and nonbridging oxygens (NBO). The number of bridging oxygens per Si tetrahedron is represented by Q^n (n = 0, 1, 2, 3, 4), [41] where Q^4 corresponds to 4 BO and 0 NBO in SiO₂ species, Q³ corresponds to 3 BO and 1 NBO in [Si₂O₅]²⁻, Q² corresponds to 2 BO and 2 NBO in [SiO₃]²⁻, Q¹ corresponds to 1 BO and 3 NBO in [Si₂O₇]⁶⁻, and Q⁰ represents 0 BO and 4 NBOs in [SiO₄]⁴ related species. Detailed insights into the different silicate species, corresponding NBOs, and wavenumber ranges (cm⁻¹) are presented in Table S1 and shown (schematically) in Fig. 1(a). In this study, Attenuated Total Reflectance – Fourier Transform Infrared Spectroscopy (ATR-FTIR) measurements are used to investigate changes in silica coordination network due to acid leaching. The bands noted between 850 and 1050 cm⁻¹ in ATR-FTIR spectra correspond to Q⁰-Q³, indicating the presence of crystalline species, while Q⁴ (1051–1250 cm⁻¹) features indicate the presence of amorphous silica. To date, there have been no studies linking the changes in the silica coordination of shales treated in

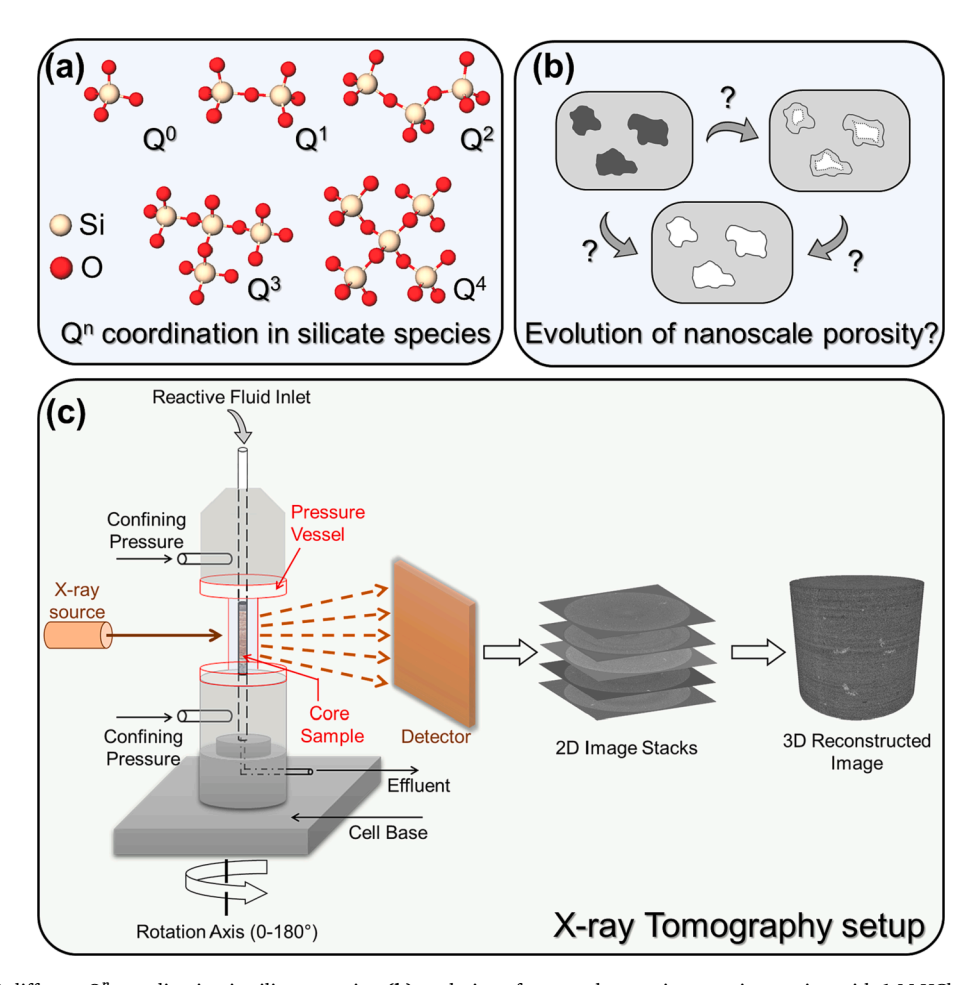


Fig. 1. Schematic of (a) different Q^n coordination in silicate species, (b) evolution of nanoscale porosity upon interaction with 1 M HCl, and (c) X-ray tomography setup used during the temporal evolution of micron-scale porosity during reaction with 1 M HCl.

acidic environments to the changes in the pore volume and temporal evolution of the porosity. Therefore, this study aims to link the changes in the siliceous matrix of shales with varying mineralogies to the nanoscale and micron-scale porosity of the reacted materials.

Shale reservoirs typically consist of varying degrees of clay content. Clays are aluminosilicate minerals, generally categorized as swelling (non-smectic) and non-swelling (smectic) clays, having 1:1 and 2:1 ratios of octahedral alumina and tetrahedral silica sheets, respectively [34,42,43]. In shale deposits, illite, kaolinite, and montmorillonite could be present [34]. The presence of clay phases can also affect the reactions in reservoirs when exposed to acids and the type of precipitates formed. Further, the dissolution kinetics of clays are different for pure clay and clays mixed with other minerals. In the presence of carbonates, the clay minerals show a relatively different trend as opposed to pure clays [44]. In the presence of carbonates, illite and kaolinite remain unaffected when reacted with HCl having concentrations up to 10 M, while the dissolution of montmorillonite has been noted due to the exchange of cations with protons leading to the formation of amorphous silica [44].

In this study, we investigate the changes in the mineralogy and morphology of silica rich-carbonate/clay lean shale (Mowry), silica, carbonate & clay bearing shale (Frontier), and silica lean – carbonate/ clay rich shale (Niobrara) reacted in 1 M hydrochloric (HCl) acid solution. While there is extensive evidence supporting increases in the pore volume of shales resulting from carbonate dissolution, the temporal evolution of porosity in silica-rich shales is due to changes in the crystalline and amorphous content of silica, and relative solubilities are investigated. Thus, the specific research questions that are addressed through this effort are: (i) How does the relative content of amorphous and crystalline silica phases differ based on the relative silica, carbonate, and clay content in shales? (ii) What is the resulting change in the pore volume of shales due to reactivity in acidic environments? (iii) What is the temporal evolution of porosity in silica-rich shales? To address these questions, changes in silica coordination and the corresponding pore volumes are determined using ATR FTIR and BET pore size measurements. In-situ X-ray microtomography measurements are harnessed to probe the evolution of porosity in shales reacted in acidic environments. Addressing these research questions sheds fundamental insights into the mineralogical and morphological evolution of heterogeneous siliceous, carbonaceous, and clay-bearing rocks and minerals for emerging applications related to the recovery of high-value elements with inherent carbon storage.

2. Materials and methods

Shale samples from three different formations which are the Mowry formation, Frontier formation, and Niobrara formation are used in the study. The shales are extracted from depths $\sim\!10,\!000$ ft (Mowry), $\sim\!12,\!000$ ft (Frontier & Niobrara), and ground to powders using 8000 M Mixer/Mill® (SPEX® Sample Prep). These powdered samples are used in the study. Further details about the composition of shale samples,

Table 1Chemical compositions of Frontier, Niobrara, and Mowry shale samples, determined using XRD, used in the study.

Content	Mowry Shale	Frontier Shale	Niobrara Shale	
	Silica Rich – Carbonate/Clay Lean	Silica, Carbonate & Clay Bearing	Silica Lean – Carbonate/Clay Rich	
Quartz (%)	72.2	43	30	
Carbonate (%)	3.9	5	12	
K-feldspar (%)	0.5	4	4	
Plagioclase (%)	9.1	7	11	
Clay (%)	5.8	38	40	
Pyrite (%)	3.7	3	3	
TOC (%)	2.25	0.92	1.71	

determined using XRD, are provided in Table 1. Based on the silica and carbonate contents of the shale samples, the samples are labeled as Silica Rich - Carbonate Lean (Mowry), Silica & Carbonate Bearing (Frontier), and Silica Lean - Carbonate Rich (Niobrara). The powder samples are reacted with 1 M HCl for 2 h in a well-stirred environment. For the reaction, 1 g of powdered sample is reacted with 100 mL of 1 M HCl. All the experiments are performed at room temperature in a glass beaker. The changes in the chemical bonding of the shale powders after the reaction are evaluated using infrared (IR) spectra, acquired in an Attenuated Total Reflection (ATR) mode using a Fourier Transform Infrared - Attenuated Total Reflection spectrometer (FTIR-ATR, Nic $olet^{TM}$ iS50, Waltham, MA). The spectra are collected in the range of 4000-650 cm⁻¹, before and after the reactions. For each spectrum, a total of 32 scans are acquired and averaged with a resolution of 2 cm^{-1} . The changes in Q⁰–Q⁴ coordination are evaluated by deconvoluting the IR spectra in the range of 850–1250 cm⁻¹ to determine changes in the silica-based species upon reaction. The deconvolution is performed using the Levenberg Marquardt algorithm using the Gaussian model embedded in Origin Pro software (OriginLab Corp.). The details about the IR data modeling are provided in **Section S1**. The acid solutions after reaction with the powdered samples are analyzed using Inductively-Coupled Plasma - Atomic Emission Spectroscopy (ICP-AES) to determine the concentrations of leached species in the solution. As a reference, 1 M HCl is also analyzed. Changes in the phase compositions and pore-solid morphology of shale samples on reaction with 1 M HCl are determined using wide-angle X-ray scattering (WAXS), and ultra-small and small angle X-ray scattering (USAXS/SAXS) measurements, respectively, performed at Sector 9-ID-C of the Advanced Photon Source (APS), Argonne National Laboratory. The unreacted and reacted samples are sandwiched between the scotch tape and placed on the measurement plate for data acquisition. The scattering from the tape is also acquired and subtracted from the data as background. During the measurements, the X-ray energy is set to 21.0 keV (corresponding to the X-ray wavelength of 0.59 Å), having a total X-ray flux of $\sim 10^{13}$ photon mm⁻² s⁻¹. The calibrations for instrument and sample-to-detector distance are performed using LaB₆ [45] for WAXS and silver behenate [46] for SAXS. The 2D area detector data are reduced and processed to 1D I(q) $v \neq (A^{-1})$ curves using *Igor* software (Wavemetrics, Lake Oswego, OR) based Nika [47] and Irena [48] macros. The size distribution profiles of pores, both open and closed, are estimated from combined USAXS-SAXS scattering curves using the maximum entropy (MaxENT) method in Irena macro [48]. Further, details about the fractal dimensions at the pore-solid interface are obtained by applying the Guinier-Porod approximation to combined USAXS/SAXS I(q) v q (Å⁻¹) curves using Beucage's approach [49]. The details about the used models and treatment of X-ray scattering data are reported in Section S2 (Supplementary Information). The variations in the mass of unreacted and reacted samples with temperature are recorded via thermogravimetric (TG) measurements, performed up to 850 °C with a ramp rate of 5 °C/min in an N₂ environment (purged at 25 mL/min) using a Thermogravimetric Analyzer (TGA, TA Instruments, SDT650, New Castle, DE). The morphologies of reacted and unreacted shale powders are imaged using a scanning electron microscope (LEO 1550 FESEM). The results from TGA and scanning electron microscopy are discussed in detail in Section S3 (Supplementary Information). The nanoscale porosity and surface areas are examined using N2 adsorption-desorption isotherms at 77 K using the Brunauer-Emmett-Teller technique (BET, Quantachrome Autosorb iQ Analyzer, Boynton Beach, FL). Finally, the changes in reactioninduced porosity in the Silica Rich - Carbonate Lean (Mowry) shale sample are determined using the time-resolved in-situ X-ray microtomography measurements using the custom-reactor, similar to the one reported by Fusseis et al. [50]. A core sample with dimensions of 3 mm in diameter and 8 mm in height is drilled out of the rock shale sample and used for the tomography measurements. The schematic of the reactor and X-ray tomography setup is presented in Fig. 1(c). The X-ray microtomography measurements are performed at the bending-magnet

2-BM-A beamline of Advanced Photon Source (APS) in Argonne National Laboratory (ANL). FLIR Oryx ORX-10G-51S5M camera with 2448 \times 2448 pixels (pixel size 3.45 $\mu m \times 3.45 \ \mu m$) is used in a fly scan mode and the projections are recorded while the sample is rotated between 0 and 180°. The data are collected on the detector region 2448 \times 1024 because of the reduced size of the X-ray beam passing the monochromator adjusted for the energy of 27 keV. The camera recorded projections from a 100 μm -thick LuAG: Ce single-crystal scintillator, magnified through a $5\times$ lens by yielding a resulting isometric voxel size of 1.3 μm . The acquisition time for each image is 66 s. The core sample is fitted in a custom cell and 1 M HCl is purged through the core for 75 min. The flow rate of the solution during the experiments is set at 0.25 mL/min. A schematic of the experimental setup is shown in Fig. 1.

These measurements coupled with the IR spectroscopic measurements, electron microscopy, and nanoscale porosity data provide detailed insights into the feedback effects of carbonate dissolution on the silica speciation in the shale samples and changes in the porosity attributed to the fine particles' mobilization upon reaction with hydrochloric acid.

3. Results and discussion

3.1. Chemical evolution in shale samples

The shale samples studied herein are extracted from deep wells and contain a variety of mineral phases. The compositions of these phases are reported in Table 1. The silica contents in Silica Rich – Carbonate/Clay Lean (Mowry) shale, Silica, Carbonate & Clay Bearing (Frontier) shale, and Silica Lean – Carbonate/Clay Rich (Niobrara) shale are 72.2 %, 43 %, and 30 %, respectively. The quartz content reported in Table 1 contains amorphous and crystalline constituents. The carbonate contents in Silica Rich – Carbonate/Clay Lean (Mowry) shale, Silica, Carbonate & Clay Bearing (Frontier) shale, and Silica Lean – Carbonate/Clay Rich (Niobrara) shale are 3.9 %, 5 %, and 12 %, respectively. The clay contents in Silica Rich – Carbonate/Clay Lean (Mowry) shale, Silica, Carbonate & Clay Bearing (Frontier) shale, and Silica Lean – Carbonate/Clay Rich (Niobrara) shale are 5.8 %, 38 %, and 40 %, respectively. The morphologies of the shales before and after reaction in acidic media are shown in Table 2 and Table 3.

Silica, Carbonate & Clay Bearing (Frontier) and Silica Lean – Carbonate/Clay Rich (Niobrara) shales have prominent carbonate bands around 712 cm $^{-1}$, 875 cm $^{-1}$, and 1450 cm $^{-1}$ [51] while Silica Rich – Carbonate/Clay Lean (Mowry) shales exhibit carbonate bands as shoulders (Fig. 2). This observation is attributed to the higher silica content in the sample, which causes the Si-O bands to dominate the IR spectrum. The bands <800 cm $^{-1}$ correspond to Si-O-Si vibrations from silicates, which is typical of quartz [52]. The vibrations between 850 and

Table 2 Specific surface areas, pore volumes, and pore sizes for unreacted and reacted shale samples are determined using the BJH method from $\rm N_2$ desorption isotherms.

Samples		Specific Surface Area (m ² /g)	Pore Volume (cc/g)	Avg. Pore Size (nm)
Silica Rich –	Unreacted	6.76	0.021	4.10
Carbonate/Clay	Reacted with	8.78	0.018	4.10
Lean (Mowry Shale)	1 M HCl			
Silica, Carbonate &	Unreacted	28.40	0.12	3.80
Clay Bearing	Reacted with	36.97	0.14	3.73
(Frontier Shale)	1 M HCl			
Silica Lean –	Unreacted	24.25	0.12	3.80
Carbonate/Clay Rich (Niobrara Shale)	Reacted with 1 M HCl	39.82	0.17	3.74

Table 3 Fractal dimensions (D_F) estimated from N_2 adsorption and Small Angle X-ray Scattering (SAXS).

Samples		$ m N_2$ adsorption NK Method	SAXS (0.003 – 0.3 Å ⁻¹)	SAXS (<0.003 Å ⁻¹)
Silica Rich	Unreacted	2.45	2.00	2.56
-Carbonate/Clay	Reacted	2.76	2.42	2.55
Lean (Mowry Shale)	with 1 M HCl			
Silica, Carbonate &	Unreacted	2.61	2.00	2.53
Clay Bearing (Frontier Shale)	Reacted with 1 M HCl	2.67	2.74	2.49
Silica Lean –	Unreacted	2.56	2.00	2.66
Carbonate/Clay Rich (Niobrara Shale)	Reacted with 1 M HCl	2.62	2.07	2.58

 $1150~\rm cm^{-1}$ are typically attributed to Si-O in $\rm SiO_4^{2^-}$ from amorphous silica, and $1430-1460~\rm cm^{-1}$ are identified as Si-O-Si vibrations [51], the detailed band assignment is presented in Table S3. After reaction with 1 M HCl, the carbonate bands (CO $_3^2$) diminish (green curves in Fig. 2) which is consistent with previously reported work [53]. As mentioned, the Si-O bands between 850 and 1150 cm $^{-1}$ are usually assigned as SiO $_4^{2^-}$ from amorphous silica.

Insights into the changes in the silica coordination behavior of shales before and after dissolution are determined from ATR FTIR analyses. For this purpose, the Si-O bands between 850 and 1250 cm⁻¹ are deconvoluted to identify Q⁰ - Q⁴ contributions before and after reaction with 1 M HCl for the silicate species by determining the number of BOs and NBOs, as discussed earlier. The deconvoluted IR bands are presented in Fig. 3. The reaction results in the dissolution of carbonate bands as indicated by the disappearance of carbonate bands between 873 and 881 cm⁻¹ in all three samples. The bands noted between 850 and 1050 cm^{-1} in ATR-FTIR spectra correspond to Q^0-Q^3 , indicating the presence of crystalline species, while Q⁴ (1051–1250 cm⁻¹) features indicate the presence of amorphous silica [54] in different shale samples. The bands in the $Q^0 - Q^3$ region shift to slightly higher wavenumbers after the reaction, which is an indication of the increase in Q³ type species upon dissolution of carbonate-rich phases in these samples. The contribution of Q⁰–Q³ and Q⁴ units in ATR-FTIR deconvoluted spectra of Silica Rich – Carbonate/Clay Lean Fig. 3(a-1, a-2), Silica, Carbonate & Clay Bearing Fig. 3(b-1, b-2), and Silica Lean – Carbonate/Clay Rich Fig. 2(c-1, c-2) shale samples, before and after the reaction, are estimated by the band area estimations and presented in Fig. 4. The bands centered at wavenumbers below $1050~\rm cm^{-1}$ are labeled as $\rm Q^0-\rm Q^3$ species, while bands centered at wavenumbers higher than $1050~\rm cm^{-1}$ are characterized as Q⁴ species [41]. For comparison, XRD patterns and IR spectra of model crystalline and amorphous silica are also presented in Figure \$1. Quartz and Silica 60 are selected as model crystalline and amorphous silica, respectively, are selected. The deconvolution of IR spectra between 850 cm⁻¹ and 1250 cm⁻¹ shows that for crystalline silica (quartz) the major Si-O vibration band centers around 1050 cm⁻¹ with the most deconvoluted bands appearing at wavenumbers <1050 cm⁻¹, while in case of amorphous silica (silica 60), the Si-O vibrations bands appear at wavenumbers higher than 1050 cm⁻¹.

Analyses of the changes in silica coordination showed that there is $<\!5$ % change in the $Q^0\!-\!Q^3$ species corresponding to the crystalline content and Q^4 content that is associated with amorphous content in Silica Rich – Carbonate/Clay Lean shale and Silica, Carbonate & Clay Bearing shale. In contrast, significant changes in the $Q^0\!-\!Q^3$ species and Q^4 content are noted in Silica Lean – Carbonate/Clay Rich shale. $Q^0\!-\!Q^3$ species increase by 34 % from 61 % in the unreacted to 95 % in the reacted shale and a corresponding decrease in Q^4 species is noted in reacted Silica Lean – Carbonate/Clay Rich shale. These results show that the amorphous content corresponding to Q^4 species dissolves

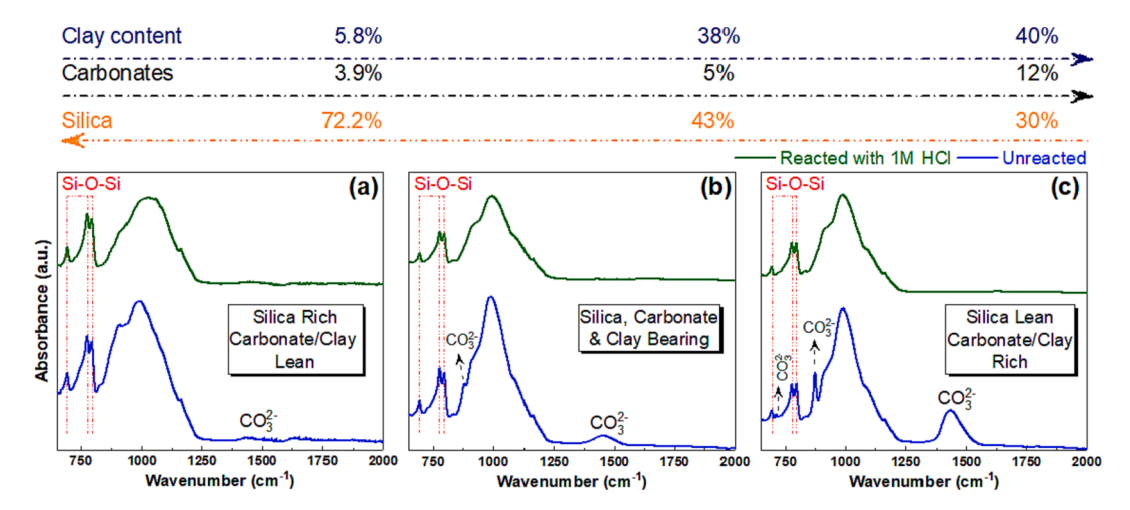


Fig. 2. Attenuated Total Reflection Infrared (ATR-IR) spectra for Silica Rich – Carbonate/Clay Lean (Mowry shale) (a), Silica, Carbonate & Clay Bearing (Frontier shale) (b), and Silica Lean – Carbonate/Clay Rich (Niobrara shale) (c) samples before and after reaction with 1 M HCl.

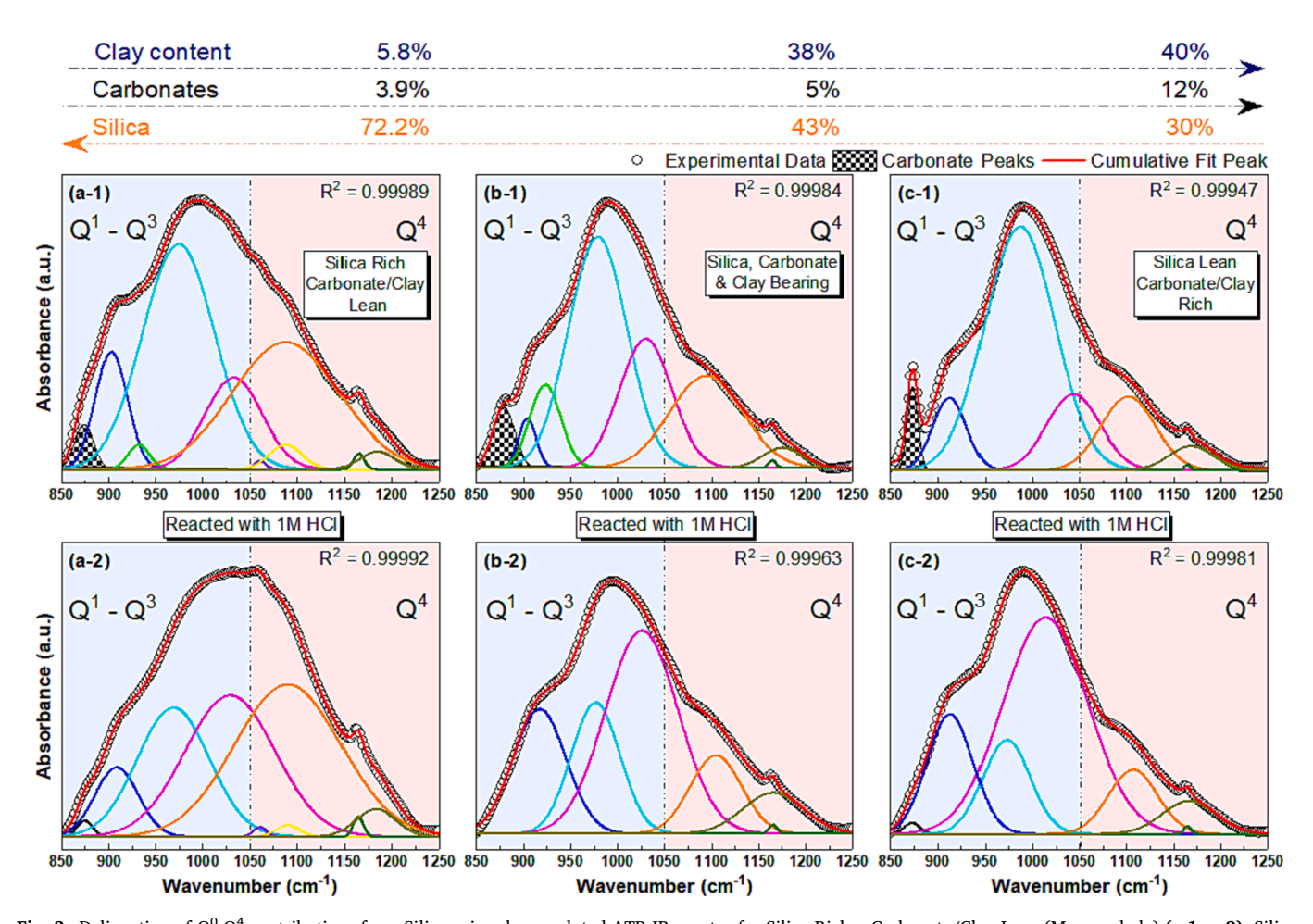


Fig. 3. Delineation of Q^0 - Q^4 contributions from Silica using deconvoluted ATR-IR spectra for Silica Rich – Carbonate/Clay Lean (Mowry shale) (a-1, a-2), Silica, Carbonate & Clay Bearing (Frontier shale) (b-1, b-2), and Silica Lean – Carbonate/Clay Rich (Niobrara shale) (c-1, c-2) unreacted and reacted with 1 M HCl, respectively. The deconvoluted peaks indicate different silicate species in the samples. (Blue, parrot, cyan, and magenta curves represent $[Si_2O_5]^{2^c}$, $[Si_2O_7]^{6^c}$ species while purple, orange, yellow, olive, and mustard curves represent $[SiO_4]^{4^c}$ species).

preferentially compared to crystalline Q^0 - Q^3 species in Silica Lean – Carbonate/Clay Rich shale. These unusual and significant changes in the silica content in Silica Lean – Carbonate/Clay Rich shale motivate us to investigate the basis for these observations.

Several hypotheses are investigated to explain the significant increase in the amorphous silica content in silica-lean shales. The first

hypothesis is that the increase in solution pH resulting from carbonate dissolution contributes to silica dissolution and reprecipitation. In the presence of a reactive fluid (e.g., HCl), a non-equilibrium chemical state exists between the shale sample and the fluid, which can lead to several reactions, including, mineral dissolution and precipitation of secondary minerals [55]. Highly acidic solutions dissolve calcium carbonate,

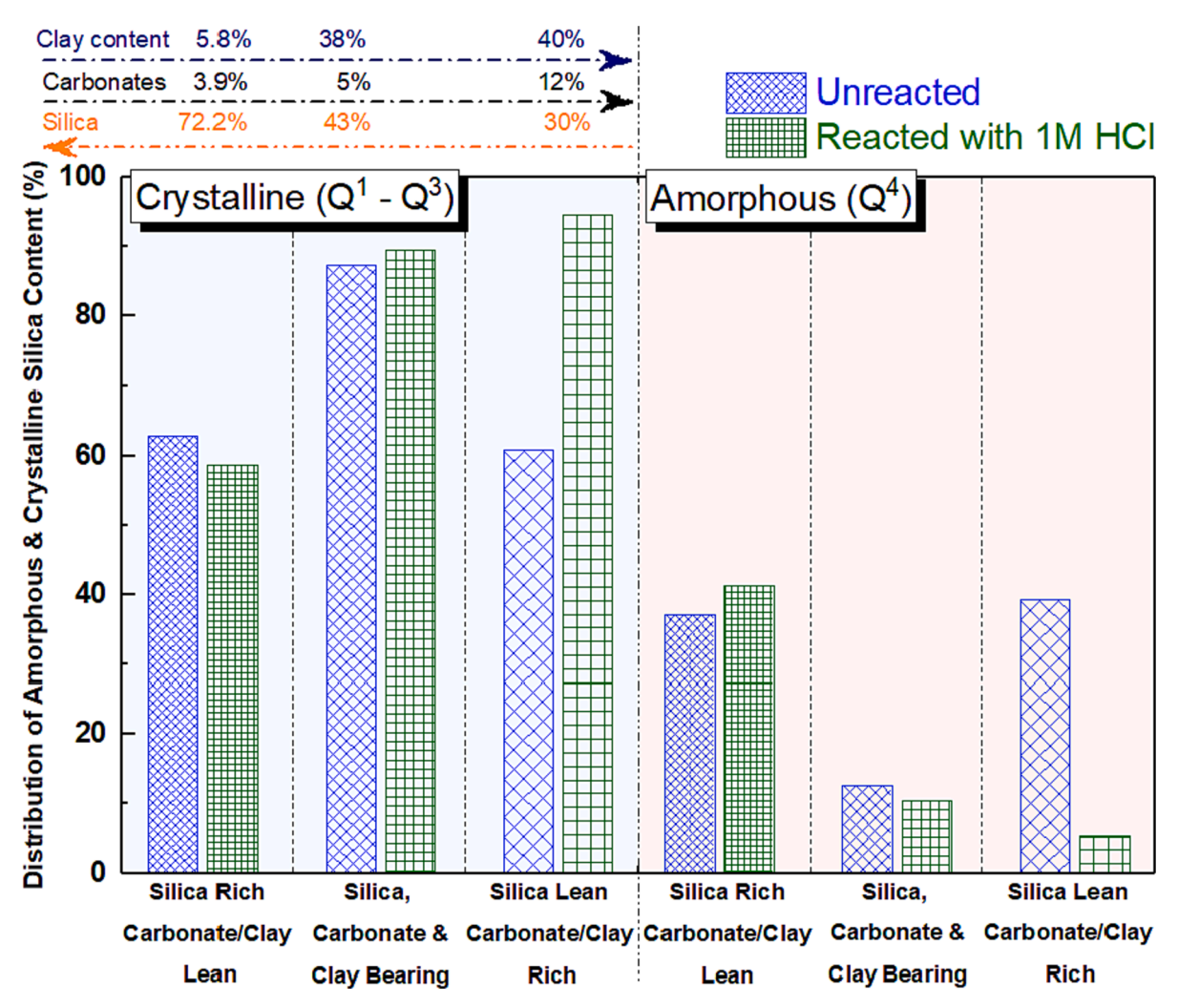


Fig. 4. Contributions of Q^0 - Q^3 and Q^4 species in unreacted and reacted (1 M HCl) Silica Rich – Carbonate/Clay Lean (Mowry shale), Silica, Carbonate & Clay Bearing (Frontier shale), and Silica Lean – Carbonate/Clay Rich (Niobrara shale) samples from the estimated band areas.

neutralize the acid, and increase the solution pH [56-58]. This increase in the solution pH enhances the solubility of silica. The corresponding changes in the crystalline phases are determined using WAXS measurements. The WAXS patterns for unreacted and reacted shale samples are presented in Fig. 5. The major phases identified are quartz [59], calcite [60], dolomite [61], clay [62,63], and pyrite [64]. Upon reaction, the peaks of calcite around 2.07 Å^{-1} and 3.36 Å^{-1} , corresponding to the (104) and (116) planes are diminished due to the dissolution of carbonate phases from all three samples. As expected, the higher peak intensity for calcite peak (~2.07 Å⁻¹) is in the Silica Lean – Carbonate/ Clay Rich (Niobrara) shale sample (Fig. 5(c-1)) compared to other samples. Moreover, the peaks of dolomite $\sim 2.18~\text{Å}^{-1}$, corresponding to the (104) plane, noted in all the unreacted samples also diminish after reaction with 1 M HCl. Carbonate dissolution is known to increase the pore size of shales [65]. The extent of carbonate dissolution during the reaction of the acid with shale is controlled by the quantity of carbonates in the shale. The carbonate mineral content of the shale formation therefore primarily determines the system's pH and controls various pHdependent reactions taking place in the shale reservoirs. In the case of the Silica Lean - Carbonate/Clay Rich shale sample, the higher carbonate content (12 %) could lead to a greater dissolution of minerals and subsequently increase the local pH of the system [66]. pH increase enables silica dissolution and results in significantly smaller amounts of amorphous silica species (Q⁴) and higher content of crystalline silicate species (Q⁰–Q³) compared to Silica Rich – Carbonate\Clay Lean and

Silica, Carbonate & Clay Bearing samples.

The second hypothesis is that chemical transformations involving clay-bearing phases contribute to silica dissolution and reprecipitation. For example, the substitution of Al³⁺ for Si⁴⁺ can shift Si-O- bands to relatively lower wavenumbers, which is noted in the case of the Silica Lean – Carbonate/Clay Rich sample, where higher numbers of NBOs are noted. Moreover, the presence of Fe and Mg sulfates and Mg phyllosilicates in silicate minerals increases the release of SiO2 into an aqueous solution, which eventually precipitates as silica or silica-rich minerals [67,68]. The modeling of low-temperature alteration of silica-rich rocks using GEOCHEQ code [69] has shown that the amorphous silica forms in secondary accumulations in acidic pHs. Further, in the presence of sulfate-rich rocks (as in the case of Silica Rich - Carbonate/Clay Lean sample), silica can deposit at low pHs because of these weathering processes. Finally, the low solubility of silica phases in the solutions with acidic pH can result in the formation of silica-rich deposits in these reservoirs in contact with acidic solutions. Moreover, the clay-rich shales (Mancos) have shown a relative decrease in the quartz content before and after the treatment with acid treatment [35]. The possible reactions in the studied samples can be identified based on the type of phases involved and their dissolution upon interaction with low pH acids (i.e., HCl) [34,35,70].

(a) Dissolution of carbonate phases

$$CaCO_{3 (s)} + 2HCl_{(aq)} \rightarrow Ca^{2+}_{(aq)} + 2Cl_{(aq)} + H_2O_{(aq)} + CO_{2 (g)}$$
 (1)

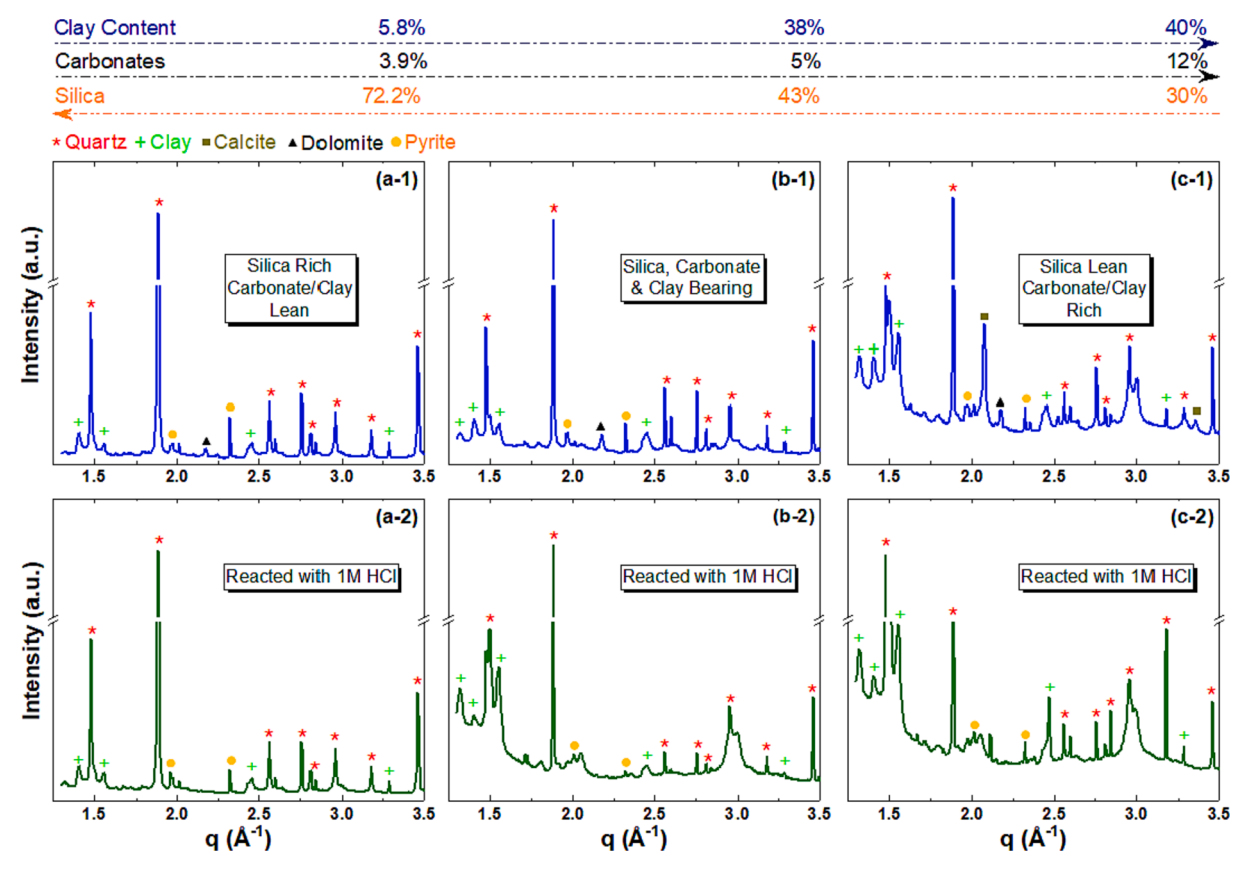


Fig. 5. Identification of different phases in Silica Rich – Carbonate Lean (Mowry shale) (a-1, a-2), Silica & Carbonate Bearing (Frontier shale) (b-1, b-2), and Silica Lean – Carbonate Rich (Niobrara shale) (c-1, c-2) samples before and after reaction with 1 M HCl, respectively, determined using the wide-angle X-ray scattering (WAXS) measurements.

$$\begin{array}{l} {\rm CaMg(CO_{3})_{2\;(s)}} + 4{\rm HCl}_{\;(aq)} \rightarrow {\rm Ca^{2+}}_{\;(aq)} + {\rm Mg^{2+}}_{\;(aq)} + 4{\rm Cl^{-}}_{\;(aq)} + 2{\rm H_{2}O}_{\;(aq)} + 2{\rm CO_{2\;(g)}} \end{array} \tag{2}$$

(b) Dissolution of pyrite phases

$$\text{FeS}_{2 \text{ (s)}} + 2\text{HCl}_{(aq)} \rightarrow \text{Fe}^{3+}_{(aq)} + 2\text{Cl}_{(aq)}^{-} + \text{H}_2\text{S}_{(g)}$$
 (3)

(c) Dissolution of clay-based phases

$$\begin{array}{c} {\rm Al}_{4}{\rm Si}_{4}{\rm O}_{10}({\rm OH})_{8\;(s)} + 12{\rm HCl}_{\;(aq)} \rightarrow 4{\rm Al}^{3+}_{\;\;(aq)} + 12{\rm Cl}_{\;\;(aq)}^{-} + 10{\rm H}_{2}{\rm O}_{\;(aq)} + {\rm SiO}_{2} \\ {}_{(s)} \end{array} \tag{4}$$

Based on the reactions above, the increased contribution of SiO_2 (Q^4 species) in Silica Rich – Carbonate/Clay Lean (Mowry) shale can be explained by the precipitation of SiO_2 in the reacted sample on the existing silica surfaces. Furthermore, the dissolution of clay-based phases leads to the formation of SiO_2 as shown in reaction 4. In our experiments, we note a monotonic increase in the crystalline silica content (Q^0 - Q^3) with higher clay content (Fig. 4). From these studies, we conclude that the higher clay and carbonate content in these shales favor the formation of crystalline silica species, while higher amorphous silica content is noted in carbonate and clay lean samples.

3.2. Fate of leached species

The concentrations of leached/dissolved elements for shale samples upon reaction with 1 M HCl are approximated using ICP measurements and presented in Fig. 6 for major species and Figure S4 for minor phases. The analysis is also performed on 1 M HCl solution in the study, for comparison. Significantly higher concentration of leached Ca is noted in the case of silica lean – carbonate/clay rich sample (620.81 mg/L) compared to other samples, i.e., 147.22 mg/L for silica, carbonate & clay bearing sample and 108.71 mg/L silica rich – carbonate/clay lean sample (Fig. 6(a)). For Mg, relatively higher leached concentration is

exhibited by silica, carbonate & clay bearing sample (71.85 mg/L) compared to silica rich - carbonate/clay lean (18.17 mg/L), and silica lean - carbonate/clay rich (37.26 mg/L) samples (Fig. 6(b)). These results are consistent with the observations from WAXS results, where calcite is dominant phase in silica lean – carbonate/clay rich sample and dolomite peaks are dominant in the silica, carbonate & clay bearing sample. The samples containing higher clay contents exhibit relatively higher leached Al content, 80.9 mg/L in silica, carbonate & clay bearing and 50.77 mg/L silica lean – carbonate/clay rich, compared to 7.75 mg/ L in silica rich – carbonate/clay lean sample (Fig. 6(c)). Similar trend is exhibited by Si, where a significantly higher amount is noted for silica, carbonate & clay bearing (45.64 mg/L), and silica lean – carbonate/clay rich (34.61 mg/L) samples, compared to 5.41 mg/L in silica rich - carbonate/clay lean sample (Fig. 6(d)). The higher amounts of leached Si in carbonate and clay rich samples also validate the hypothesis that a local increase in the pH, upon dissolution of carbonate phases favors silica dissolution. Moreover, the significantly lower amount of leached Si in silica rich – carbonate/clay lean sample also indicates the reprecipitation of Si as amorphous silica as noted from increased Q⁴ vibrations in the reacted sample (Fig. 4). We also note that higher content of leached potassium from silica, carbonate & clay bearing (70.13 mg/L), and silica lean - carbonate/clay rich (54.73 mg/L) samples, which contain higher clay contents, compared to silica rich - carbonate/clay lean sample, where only 4.55 mg/L of leached K is noted (Fig. 6(e)). A similar trend is noted for Ba, where Ba can be present in the clay matrix or as a substituent for K⁺ in K-feldspars [71,72]. Clay and pyrite minerals are the sources of small quantities of Fe in the leached solutions (Fig. 6(f)) [34]. Finally, we also note relatively higher leached amounts of S (15.35 mg/ 1) and P (28.60 mg/L) in the silica rich – carbonate/clay lean sample indicating the dissolution of pyrite and K-feldspar phases in the sample, which also favors the precipitation of amorphous silica phases.

Mowry = Silica Rich - Carbonate/Clay Lean Frontier = Silica, Carbonate & Clay Bearing Niobrara = Silica Lean - Carbonate/Clay Rich

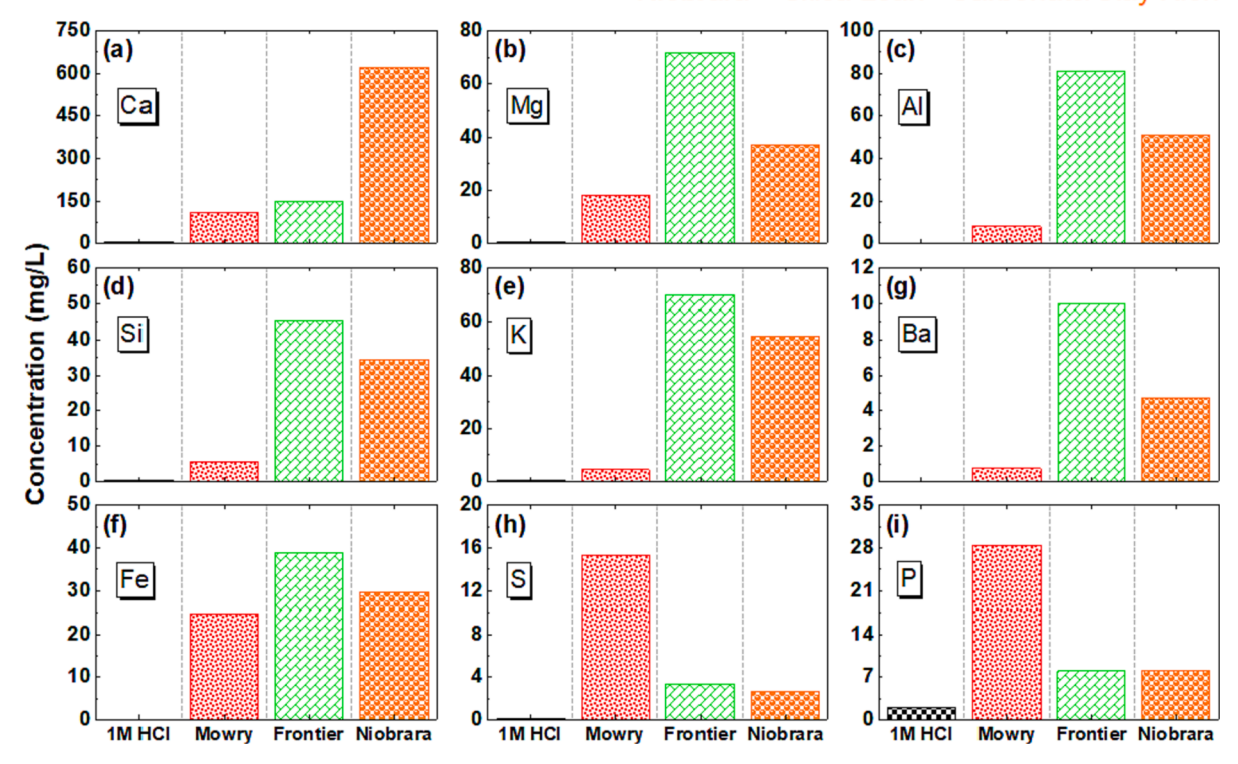


Fig. 6. The concentration of different leachates from shales samples upon reaction with 1 M HCl (1 g powder per 100 mL solution) at room temperature for 2 h.

Prior studies have shown that the injection of reactive (acidic) fluids can create nonuniform surface etching along the fracture surfaces in the shale samples [73] and impact the porosity and permeability of reservoirs. Carbonate dissolution in these systems releases fine particles (also called fines) of minerals such as K-feldspar [74], which can migrate within the reservoir and cause pore blockage. The effect of carbonate dissolution on the nanoscale morphology of these shale samples upon reaction with 1 M HCl is determined using gas adsorption—desorption measurements as discussed in the following section.

3.3. Changes in nanoscale pore morphology of shales

Detailed insights into the changes in the pore volumes and specific surface area are obtained from BET N₂ adsorption-desorption isotherms. The isotherms, pore size distribution (PSD) curves, and cumulative pore volumes of unreacted and reacted shale samples are presented in Figure S6, and Fig. 7, respectively. It is interesting to note that the cumulative pore volumes of the shales reacted in silica, carbonate, and clay-bearing shales and silica lean, carbonate and clay-rich shale increases when reacted in acids unlike silica-rich shales (Fig. 7). This can be attributed to the higher carbonate and clay contents in these samples, which results in higher dissolution of this mineral content upon reaction with 1 M HCl. The pore volume contributions arise from changes in the pores having sizes greater than 4 nm for silica rich – carbonate/clay lean shale sample (Fig. 7(a-1)), where the pore volume in the size range of 4 – 60 nm is increased and that greater than 60 nm is slightly decreased. Based on this observation, it is inferred that the mineral components (carbonate/clay) reside in these pores (<60 nm) and their dissolution causes a small increase in the pore volumes in this range, while the precipitation of secondary phases occurs along the walls of relatively larger pores (>60 nm). For silica, carbonate, and clay bearing sample (Fig. 7(b-1)) and silica lean – carbonate/clay rich sample (Fig. 7(c-1)),

the slight increase in the pore volumes after the reaction is attributed to the dissolution of carbonate and clay-based phases. For example, the cumulative pore volume of silica rich – carbonate/clay lean shale decreases by $14.2\,\%$. However, for silica, carbonate, and clay-bearing, and silica lean – carbonate/cay lean shales the cumulative pore volumes increase by $16.67\,\%$, and $41.67\,\%$, respectively, compared to the unreacted shales.

Furthermore, a significant increase in the surface area and rougher interfaces is noted in the dissolution and precipitation of silica species. For example, the surface areas of silica-rich, silica, carbonate and claybearing, and silica-lean shales increased by 29.88 %, 30.17 %, and 64.21 %, respectively, compared to the unreacted shales. The relatively higher increase in the surface area and pore volume after reaction with 1 M HCl for Silica Lean – Carbonate/Clay Rich sample can be attributed to the higher carbonate (12 %) and clay (40 %) content compared to Silica, Carbonate & Clay Bearing sample (5 % carbonate, 38 % clay) and Silica Rich – Carbonate/Clay Lean (3.9 % carbonate, 5.8 % clay) sample. The decrease in the average pore size of Frontier and Niobrara shale samples is attributed to the dissolution of carbonate/clay-based phases.

The gas adsorption measurements provide information about the open or available pores in the samples. Comprehensive insights into the closed and open pores of these materials are obtained using ultra-small and small-angle X-ray scattering (USAXS/SAXS) measurements. The combined USAXS/SAXS curves and corresponding pore size distributions for samples before and after reaction with 1 M HCl are presented in Fig. 8. Data fit and models used for these analyses are reported in Section S1 (Supplementary Information). The interlayer spacings emerging from clay content in the sample are noted at higher q-values. For instance, the peaks $\sim 0.75~\mbox{Å}^{-1}$ corresponding to the d-spacing of 8.4 Å diminish after the reaction (see insets in Fig. 8(a-1), (b-1), and (c-1)). These observations indicate the collapse of interlayer spacing upon reaction, which could be caused by the leaching of cations from the

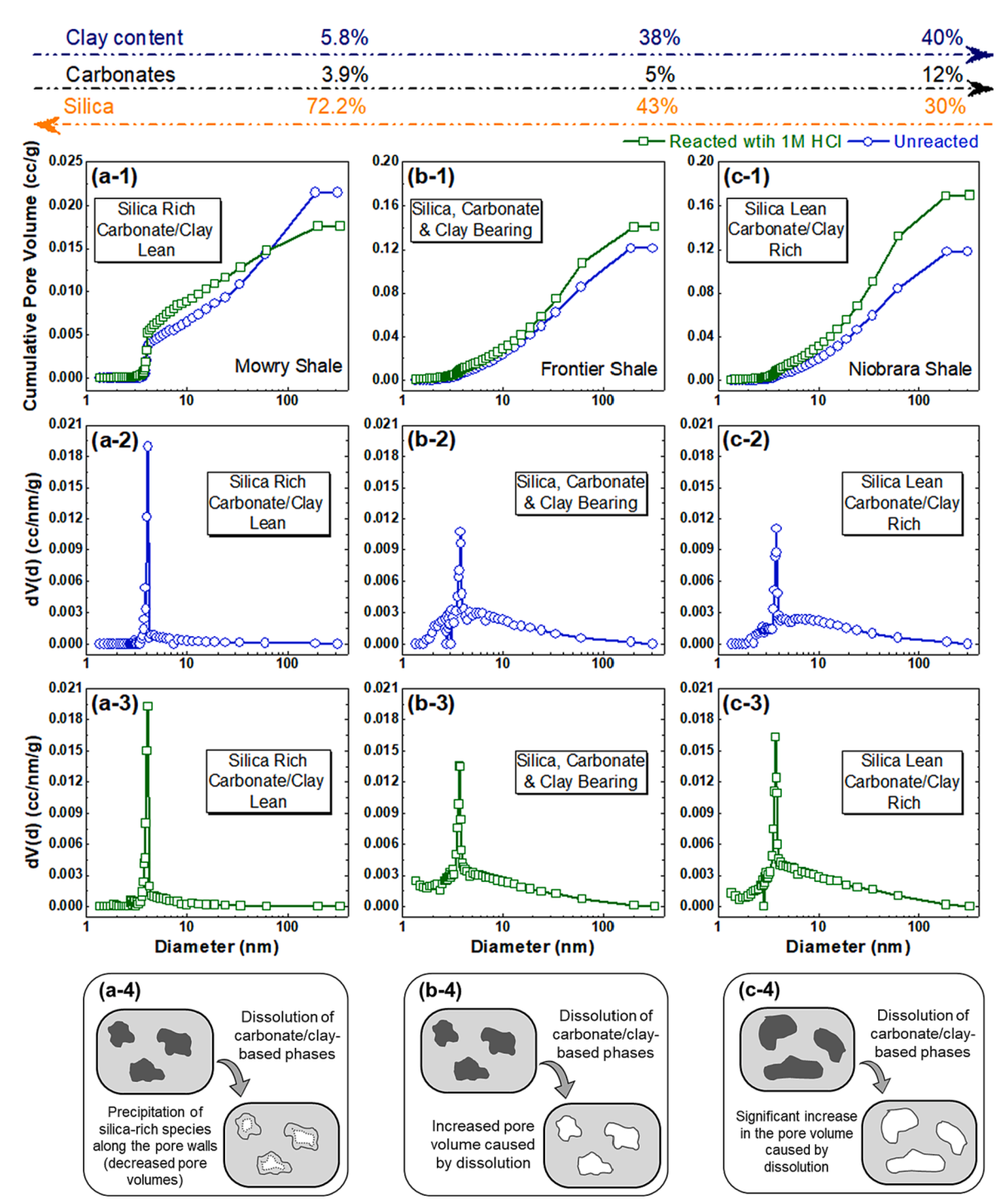


Fig. 7. Cumulative pore volumes and pore size distributions of Silica Rich – Carbonate/Clay Lean (Mowry shale) (a-1, a-2, a-3), Silica, Carbonate & Clay Bearing (Frontier shale) (b-1, b-2, b-3), and Silica Lean – Carbonate/Clay Rich (Niobrara shale) (c-1, c-2, c-3) samples before and after reaction with 1 M HCl, respectively, determined using Barrett-Joyner-Halenda (BJH) method applied on the desorption isotherm.

interlayers, which also results in silica formation. Further, the pore volume distributions are evaluated by normalizing the volume distributions of each sample. This approach can help us estimate the relative abundance of pores within each sample. In the case of the Silica Rich – Carbonate/Clay Lean sample, the unreacted sample has a relatively higher number of larger mesopores (10–30 nm) and these pores decrease in number after reaction with 1 M HCl. Moreover, a small shift in the pore sizes is noted which could indicate the precipitation of new phases along the pore walls.

For Silica, Carbonate & Clay Bearing sample, a significant decrease in

the relatively large mesopores (10–20 nm) is noted, while the size of the average mesopores is increased slightly (\sim 5 nm to \sim 8 nm) after the reaction. This observation can be attributed to the dissolution of carbonate phases in the sample residing in these pores and the dissolution of the clay phases. Moreover, an increase in larger mesopores sizes is noted (>25 nm). In the case of the Silica Lean – Carbonate/Clay Rich sample, the relative abundance of smaller mesopores (\sim 5 nm) remains consistent, while the pores with sizes \sim 20 nm are diminished and either become large (\sim 25 nm) or decrease in size as can be noted by the increase in the relative abundance of pores having sizes \sim 12 nm. Finally,

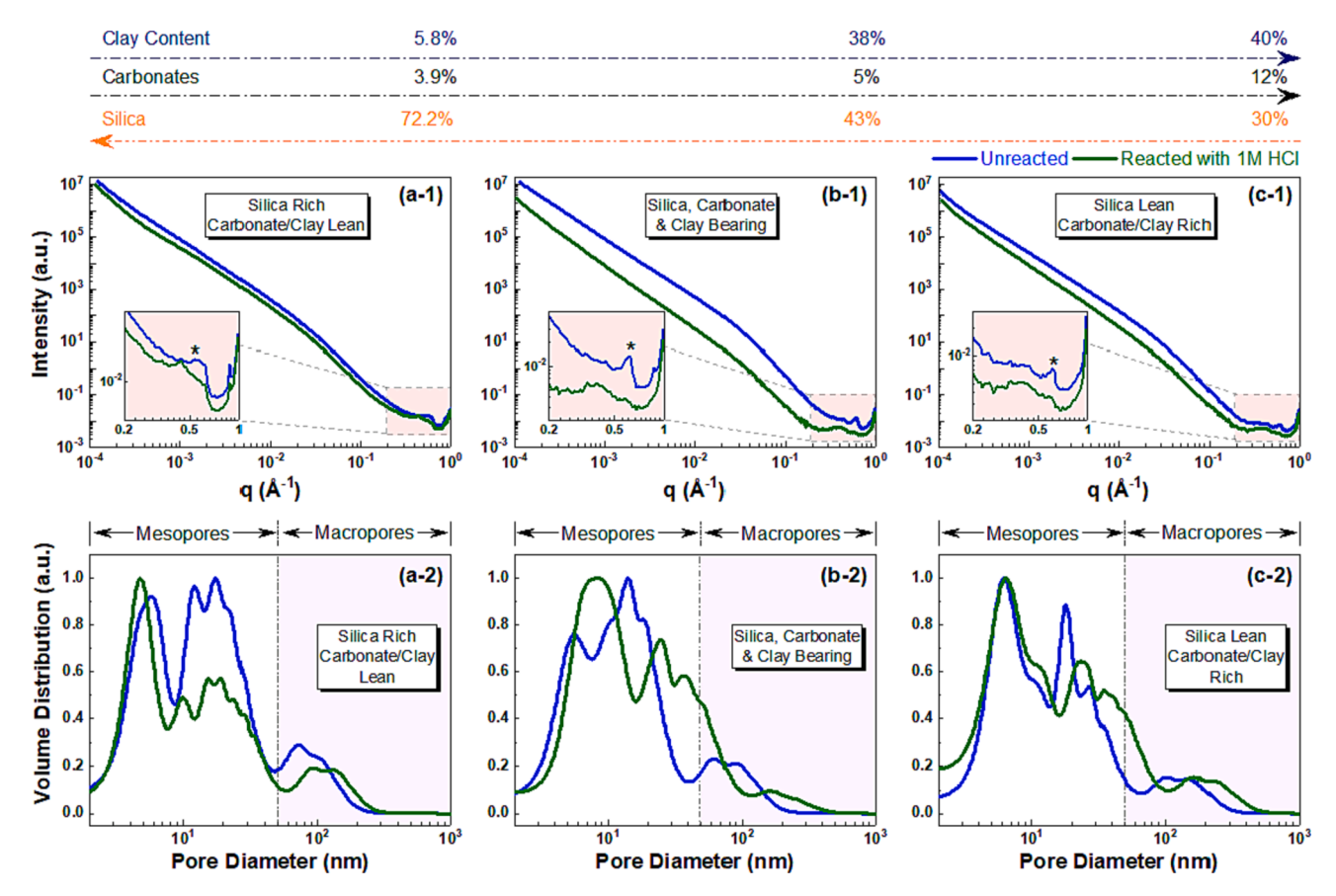


Fig. 8. Combined USAXS/SAXS curves for (a-1) Silica Rich – Carbonate/Clay Lean, (b-1) Silica, Carbonate & Clay Bearing, and (c-1) Silica Lean – Carbonate/Clay Lean samples. The corresponding pore size distributions obtained from fitting the USAXS/SAXS curves are presented in panels (a-2), (b-2), and (c-2).

the size of macropores increases slightly after the reaction for all samples. The relative abundance of macropores decreases slightly for Silica Rich – Carbonate/Clay Lean sample, while a prominent decrease is noted in the case of the Silica, Carbonate & Clay Bearing sample. However, for Silica Lean – Carbonate/Clay Rich sample, the relative abundance of macropores remains somewhat similar. The noted increase in relatively larger mesopores and macropores for samples containing higher carbonate and clay content after the reaction is consistent with the increased pore volumes and surface areas for these samples.

Further, the fractal dimensions at the pore-solid interface are determined from the power-law exponent (P) using a unified fitting approach based on Beaucage's method [49] (details in Section S1). The fractal dimensions are evaluated in two population regions in our data: population 1 between 0.003 $\mbox{\normalfont\AA}^{-1}$ and 0.3 $\mbox{\normalfont\AA}^{-1},$ and population 2 at qvalues $< 0.003 \text{ Å}^{-1}$. The P values for samples before and after the reaction lie between 3 and 4, indicating the presence of surface fractals (D_s) , and $D_s = 6$ -P. The changes in D_s upon reaction are presented in Fig. 9. For population 1, D_s value for all three samples is 2, which indicates scattering from a smooth pore-solid interface [75]. After reaction with 1 M HCl, D_s values increase to 2.42 and 2.47 for Silica Rich -Carbonate/Clay Lean and Silica, Carbonate & Clay Bearing samples, respectively. Only a small increase (D_s = 2.07) is noted for Silica Lean -Carbonate/Clay Rich sample. This increase in the value indicates a slight increase in the roughness at the pore-solid interface. The scattering in this range (for population 1) is attributed to the features at interfaces of pores sized between 2.1 nm and 209.4 nm i.e., mesopores and macropores. The increased roughness can be attributed to the dissolution of matter, and precipitation of new phases along pore walls. The observations of a relatively higher increase in roughness at the pore-solid interface for Silica Rich - Carbonate/Clay Lean and Silica, Carbonate & Clay Bearing samples compared to Silica Lean - Carbonate/Clay Rich sample are consistent with the changes in pore size distributions obtained from X-ray scattering (Fig. 7). Moreover, the fractals at low q-values ($<0.003~\text{Å}^{-1}$), which correspond to features larger than $\sim\!210$ nm, show a slight increase in values, meaning that the pore-solid interfaces for larger pores became smoother after the reaction. The increase, although not significant across the samples, becomes more prominent with the decreasing silica and increasing carbonate/clay contents.

Finally, to understand the changes in the microscale porosity during the reaction of the Silica Rich – Carbonate/Clay Lean (Mowry) shale sample with 1 M HCl, *in-situ* X-ray microtomography measurements are performed. These results are discussed in detail in the following section.

3.4. Evolution of microscale porosity via in-situ microtomography

The changes in microscale porosity of Silica Rich – Carbonate/Clay Lean (Mowry) shale core are determined using time-resolved X-ray microtomography measurements. These measurements are performed when 1 M HCl is in continuous contact with the solid sample at a constant fluid flow rate of 0.25 mL/min in a triaxial cell [76]. The 2D stack images, collected on the detector, are reconstructed using Object Research System (ORS) Dragonfly software [77] to obtain the 3D images of the core sample. The images of the Silica Rich – Carbonate Lean core sample at the start (0 min), after 25 min, 50 min, and 75 min of reaction time are processed and presented in Fig. 10(a). The color scheme is selected to show a better contrast between the core sample and porosity in the sample. The grayscale images of represented samples are shown in Figure S7. The porosity changes are determined by pixel analysis on the X-ray microtomography images. The voids (dark pixels), representing the total porosity, in the core sample, are labeled as microscale pores as shown in Fig. 10(a-1). The changes in the porosity are determined by

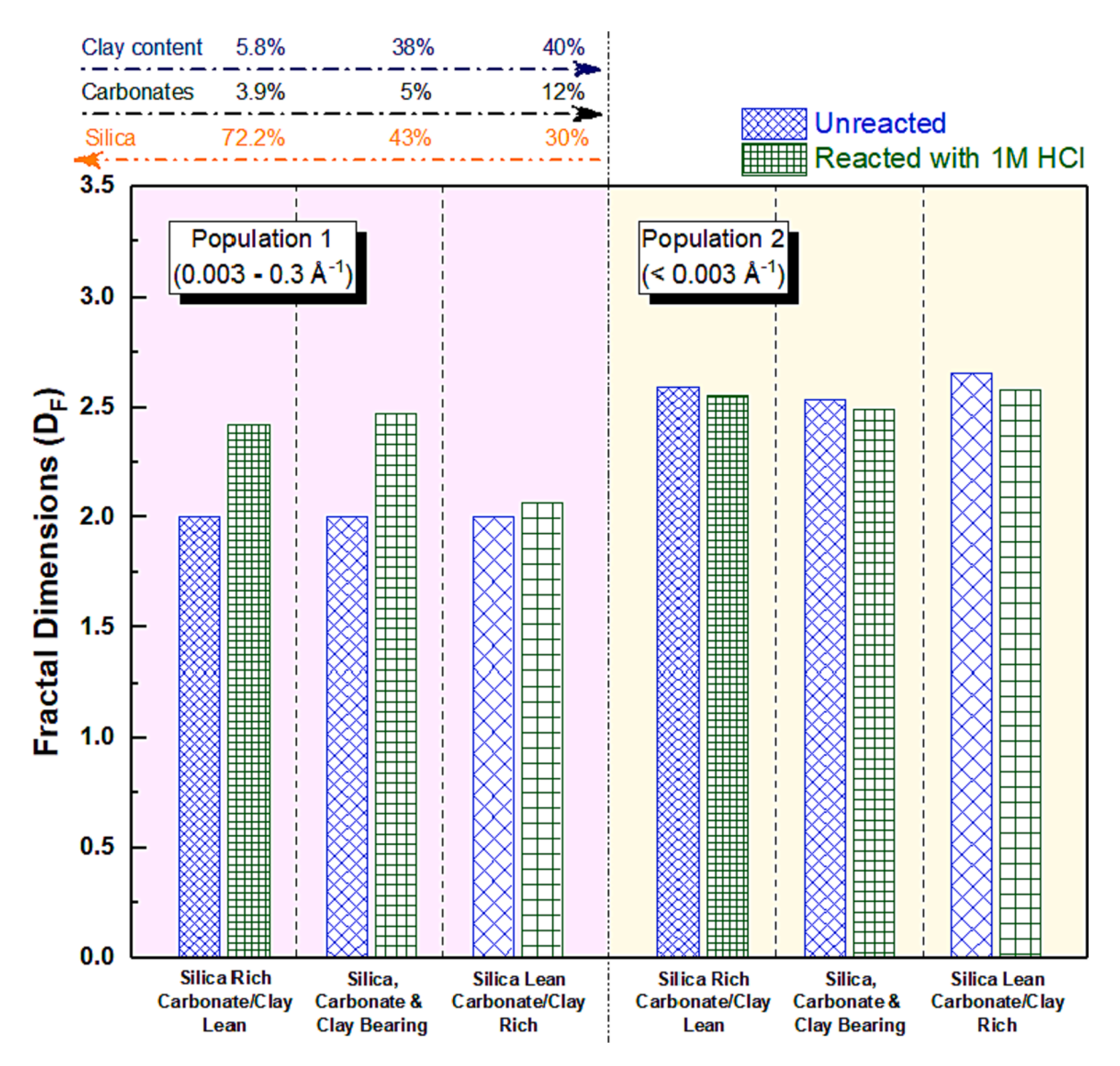


Fig. 9. Fractal dimensions of unreacted and reacted shale samples are estimated from combined USAXS/SAXS data at two different length scales. Population 1 and population 2 represent the scattering from pores having dimensions 2–200 nm and larger than 200 nm, respectively.

analyzing changes in the pixel percentage (%) of voids during the reaction. The evolution of flow channels is estimated by analyzing the connected voids (pixels). The large void bodies connected via 6 pixels and 26 pixels (available options in the software) are analyzed to estimate the changes in small and large flow channels, respectively, as shown in Fig. 10(a-2) and (a-3). The estimated changes in the total porosity and channels connected via 6 pixels and 26 pixels are presented in Fig. 10(b).

Non-monotonic temporal evolution of the porosity of the reacted shales is noted. Dissolution of carbonate/clay-based phases in the shale sample causes the porosity to increase after the first 25 min. At 50 min and 75 min, sedimentation of amorphous silica (SiO $_2$) species as the reaction proceeds reduces the total porosity. Briefly, the total porosity increases from 6.7 % to 10.7 % after 25 min of reaction with 1 M HCl. The percentage of channels connected via 6 pixels increases from 2.6 % to 6.8 %, while that for 26 connected pixels increases from 3.1 % to 8.2 %. However, after 50 min, a decrease in the porosity of the shale core is noted. The total porosity is decreased to 4.24 % and 4.02 % after a reaction time of 50 min and 75 min, respectively. Moreover, a decrease in the percentage of channels connected via 6 pixels and 26 pixels is also noted. The percentage of smaller channels (6 pixels) decreases to 0.95 %

and 0.77 %, while the percentage of relatively large channels decreases to 1.33 % and 1.16 % after 50 min and 75 min of reaction time, respectively (Fig. 10(a-2)). This evolution in porosity is attributed to the mobilization of precipitated fine particles and fines released due to carbonate dissolution [74] under the applied flow rate (0.25 mL/min). These fine particles not only decrease the overall porosity of the core sample but can also move within the developed flow channels freely, which is noted by the differences in the channels (connected by the pixel size of 6) at 50 min and 75 min (Fig. 10(a-2)). These mobilized fine particles contribute to pore plugging in these reservoir rocks and may have a direct effect on the accessibility of these pore spaces for applications related to CO_2 storage.

Based on these observations, we propose the mechanism of phase dissolution, silica speciation/precipitation, and resulting rougher pore-solid interfaces in Fig. 11. Initially, the dissolution of carbonate/clay phases increases the porosity in silica-rich shales. Over time, the precipitation of fine particles in acidic environments (which are typically silica particles) reduces the pore volume and enhances the surface roughness. Amorphous silica is more labile and soluble compared to crystalline silica [78,79].

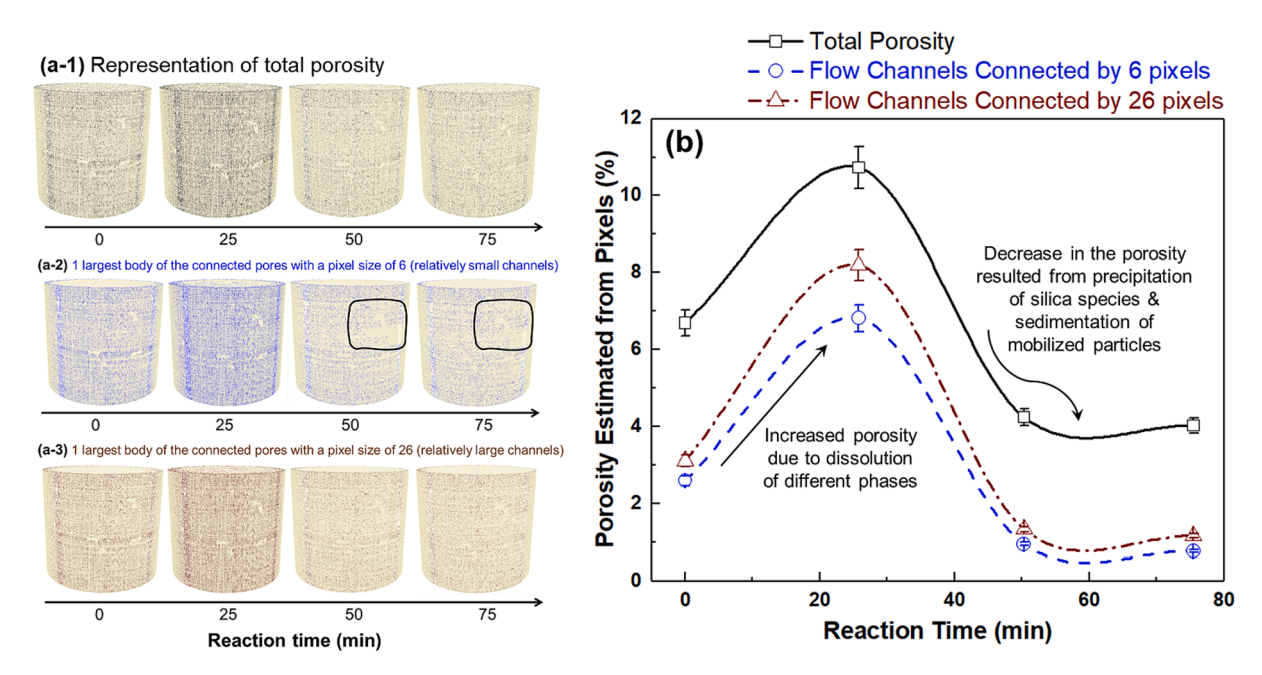


Fig. 10. X-ray microtomography images of core sample drilled out of (Silica Rich – Carbonate/Clay Lean) Mowry shale sample. The darker (black) spots (a-1) indicate the total porosity in the sample. Pore channels connected via 6 pixels (a-2), and 26 pixels (a-3) are also presented. The diameter of the core presented is 2.64 mm and the pixel size is 1.3 μm. Porosity estimated from pixel (%) as a function of reaction time estimated from the X-ray tomography image analysis (b). The changes in the channel positions at 50 min and 75 min indicate that the local porosity evolves as the reaction proceeds, governed by the mobilization of precipitated particles. The highlighted regions in (a-2) indicate the changes in the flow channels originating from the movement of precipitated fine particles.

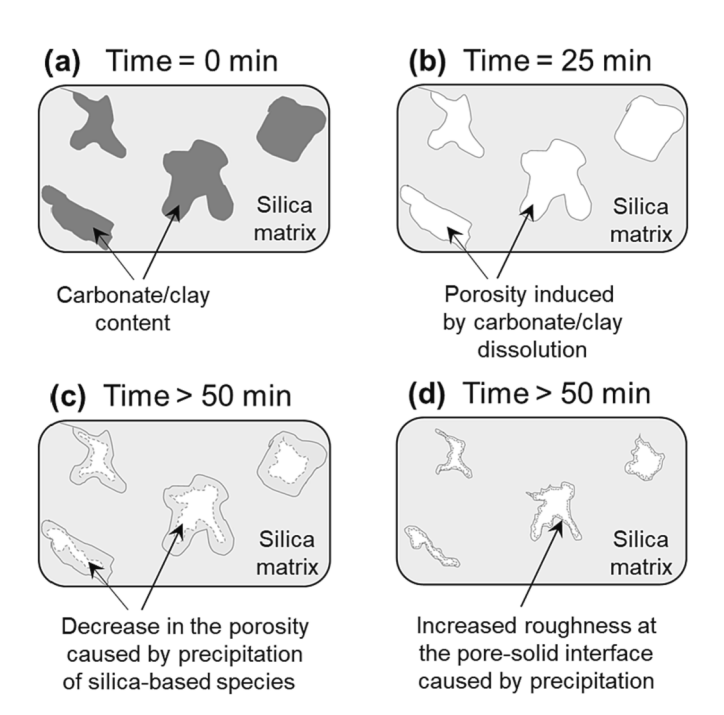


Fig. 11. Schematic representation of changes in the porosity of shale sample during reaction with 1 M HCl. The carbonate/clay phases are present in the silica-rich matrix (a), the porosity of the sample increases upon dissolution of these phases within the first 25 min of reaction (b), precipitation of silica-based species causes the porosity to decrease as the reaction proceeds (c), and porosity changes caused by the mobilization of fine particles (d).

4. Conclusions

Investigation of the feedbacks of mineralogical heterogeneity on the chemistry and morphology of shale samples in acidic environments shows that dissolution and reprecipitation of amorphous silica in silica-

rich shales reduce the porosity of these materials. These studies show that highly acidic environments such as those created by wet supercritical CO2 can have vastly different impacts on shales based on differences in mineralogy. The amorphous content of silica in silica-lean and carbonate-rich shales is significantly reduced while the corresponding crystalline content is enhanced. The increase in amorphous silica content relative to crystalline content in silica-rich shales is attributed to the dissolution of clays and the resulting precipitation of amorphous silica particles and increases in solution pH resulting from carbonate dissolution which local silica dissolution, which then reprecipitate in a bulk acidic fluid. Pore volume and surface area are considerably higher in the reacted silica-lean and silica-bearing shales due to the abundance of reactive carbonate and clay phases. Nonmonotonic evolution of the porosity in silica-rich shales is attributed to the initial dissolution and reprecipitation of particulate matter. Even though the conventional understanding is that silica is unreactive in acidic environments, our findings suggest that the dissolution and reprecipitation of siliceous matter influence the nano-scale and micronscale morphology and the evolution of flow paths in these heterogeneous material systems. Incorporating these non-monotonic temporal effects underlying the morphological evolution of these heterogeneous systems is crucial for developing predictive controls over the fate of fluids in subsurface reservoirs with mineralogical heterogeneity for applications related to sustainable subsurface energy technologies.

Credit Author Statement

G. G. conceptualized the study, organized and edited the manuscript. H. A. conducted the experiments and wrote the manuscript. S. A. and P. V. D. supported X-ray tomography measurements. A. A. and J. K. supplied the materials and contributed to the characterization of the unreacted materials.

Declaration of Competing Interest

The authors declare the following financial interests/personal relationships which may be considered as potential competing interests:

Greeshma Gadikota reports financial support was provided by DOE - Office of Basic Energy Science.

The remaining authors declare that they have no known competing financial interests or personal relationships that could have appeared to influence the work reported in this paper.

Data availability

Data will be made available on request.

Acknowledgments

This work was supported by the EFRC-MUSE, an Energy Frontier Research Center funded by the U.S. Department of Energy, Office of Science, Basic Energy Sciences under Award #DE-SC0019285. The use of the Advanced Photon Source, an Office of the Science User Facility operated for the U.S. Department of Energy (DOE) Office of Science by Argonne National Laboratory, is supported by the U.S. DOE under Contract DE-AC02-06CH11357. This work made use of the electron microscopy facility of the Cornell Center for Materials Research (CCMR) with support from the National Science Foundation Materials Research Science and Engineering Centers (MRSEC) program (DMR-1719875).

Appendix A. Supplementary data

Supplementary data to this article can be found online at $\frac{\text{https:}}{\text{doi.}}$ org/10.1016/j.fuel.2022.127144.

References

- [1] Bachu S. Sequestration of CO₂ in geological media in response to climate change: road map for site selection using the transform of the geological space into the CO₂ phase space. Energy Convers Manag 2002;43:87–102.
- [2] Kashim MZ, Tsegab H, Rahmani O, Abu Bakar ZA, Aminpour SM. Reaction mechanism of wollastonite in-situ mineral carbonation for CO₂ sequestration: effects of saline conditions, temperature, and pressure. ACS Omega 2020;2020.
- [3] Gadikota G, Matter J, Kelemen P, Brady PV, Park AHA. Elucidating the differences in the carbon mineralization behaviors of calcium and magnesium bearing alumino-silicates and magnesium silicates for CO₂ storage. Fuel 2020;277:117900.
- [4] Gadikota G, Matter J, Kelemen P, Park A-H-A. Chemical and morphological changes during olivine carbonation for CO₂ storage in the presence of NaCl and NaHCO₃. Phys Chem Chem Phys 2014;16.
- [5] Kelemen PB, Aines R, Bennett E, Benson SM, Carter E, Coggon JA, et al. In-situ carbon mineralization in ultramafic rocks: natural processes and possible engineered methods. Energy Procedia 2018;146:92–102.
- [6] Liu Y, Wang W, Gu L, Wang Y, Ying Y, Mao Y, et al. Flexible CuO nanosheets/ reduced-graphene oxide composite paper: binder-free anode for high-performance lithium-ion batteries. ACS Appl Mater Interfaces 2013;5:9850-5.
- [7] Agartan E, Gaddipati M, Yip Y, Savage B, Ozgen C. CO₂ storage in depleted oil and gas fields in the Gulf of Mexico. Int J Greenh Gas Control 2018;72:38–48.
- [8] Strapoć D, Mastalerz M, Schimmelmann A, Drobniak A, Hasenmueller NR. Geochemical constraints on the origin and volume of gas in the new albany shale (Devonian-Mississippian), Eastern Illinois Basin. Am Assoc Pet Geol Bull 2010;94: 1713–40.
- [9] Bachu S, Bonijoly D, Bradshaw J, Burruss R, Holloway S, Christensen NP, et al. CO₂ storage capacity estimation: methodology and gaps. Int J Greenh Gas Control 2007; 1:430–43.
- [10] Kharaka YK, Cole DR, Thordsen JJ, Kakouros E, Nance HS. Gas-water-rock interactions in sedimentary basins: CO₂ sequestration in the Frio Formation, Texas, USA. J Geochemical Explor 2006;89:183–6.
- [11] Nuttal BC, Eble C, Bustin RM, Drahovzal JA. Analysis of Devonian black shales in Kentucky for potential carbon dioxide sequestration and enhanced natural gas production. Greenh Gas Control Technol 2005:2225–8.
- [12] Gadikota G, Park A, Hyung A. Accelerated carbonation of Ca- and Mg-bearing minerals and industrial wastes using CO₂. Carbon Dioxide Util 2015:2225–8.
- [13] Zhang N, Chai YE, Santos RM, Siller L. Advances in process development of aqueous CO₂ mineralisation towards scalability. J Environ Chem Eng. 2020;8.
- [14] Liu M, Asgar H, Seifert S, Gadikota G. Novel aqueous amine looping approach for the direct capture, conversion and storage of CO₂ to produce magnesium carbonate. Sustain Energy Fuels 2020;4:1265–75.
- [15] Liu M, Gadikota G. Single-step, low temperature and integrated CO₂ capture and conversion using sodium Glycinate to produce calcium carbonate. Fuel 2020;275: 117887.
- [16] Liu M, Gadikota G. Integrated ${\rm CO_2}$ capture, conversion, and storage to produce calcium carbonate using an amine looping strategy. Energy Fuel 2018.

[17] Ampomah W, Balch R, Cather M, Rose-coss D, Dai Z, Heath J, et al. Evaluation of CO₂ storage mechanisms in CO₂ enhanced oil recovery sites: application to morrow sandstone reservoir. Energy Fuel 2016;30:8545–55.

- [18] Rezk MG, Foroozesh J, Zivar D, Mumtaz M. CO₂ storage potential during CO₂ enhanced oil recovery in sandstone reservoirs. J Nat Gas Sci Eng 2019;66:233–43.
- [19] Carroll SA, Mcnab WW, Dai Z, Torres SC. Reactivity of mount simon sandstone and the eau Claire shale under CO₂ storage conditions. Environ Sci Technol 2013;47: 252–61.
- [20] Koukouzas N, Kypritidou Z, Purser G, Rochelle CA, Vasilatos C, Tsoukalas N. Assessment of the impact of CO₂ storage in sandstone formations by experimental studies and geochemical modeling: the case of the Mesohellenic Trough, NW Greece. Int J Greenh Gas Control 2018;71:116–32.
- [21] Uzun O, Kazemi H. Assessment of enhanced oil recovery by osmotic pressure in unconventional reservoirs: application to Niobrara chalk and Codell sandstone. Fuel 2021;306;121270.
- [22] Memon A, Li A, Jacqueline N, Kashif M, Ma M. Study of gas sorption, stress effects and analysis of effective porosity and permeability for shale gas reservoirs. J Pet Sci Eng 2020;193:107370.
- [23] Wei B, Zhang X, Liu J, Xu X, Pu W, Bai M. Adsorptive behaviors of supercritical CO₂ in tight porous media and triggered chemical reactions with rock minerals during CO₂-EOR and -sequestration. Chem Eng J 2020;381:122577.
- [24] Zhang X, Wei B, Shang J, Gao K, Pu W, Xu X, et al. Alterations of geochemical properties of a tight sandstone reservoir caused by supercritical CO₂-brine-rock interactions in CO₂-EOR and geosequestration. J CO₂ Util 2018;28:408–18.
- [25] Van Der ML, Hofstee C, Orlic B. The fluid flow consequences of CO₂ migration from 1000 to 600 metres upon passing the critical conditions of CO₂. Energy Procedia 2009;1:3213–20.
- [26] Lyu Q, Tan J, Li L, Ju Y, Busch A. The role of supercritical carbon dioxide for recovery of shale gas and sequestration in gas shale reservoirs. Energy Environ Sci 2021;14:4203–27.
- [27] U. S. Energy Information Administration (EIA). How Much Shale Gas is Produced in the United States?; EIA: Washington D.C., 2018; https://www.eia.gov/tools/fa qs/faq.php?id=907&t=8.
- [28] Schaef HT, Davidson CL, Owen AT, Miller QRS, John S, Thompson CJ, et al. CO₂ utilization and storage in shale gas reservoirs: experimental results ANF economic impacts. Energy Procedia 2014;63:7844–51.
- [29] Khosrokhavar R, Griffiths S, Wolf K. Shale gas formations and their potential for carbon storage: opportunities and outlook. Environ Process 2014;1:595–611.
- [30] Louk K, Ripepi N, Luxbacher K, Gilliland E, Tang X, Keles C, et al. Monitoring CO₂ storage and enhanced gas recovery in unconventional shale reservoirs: results from the Morgan county, Tennessee injection test. J Nat Gas Sci Eng 2017;45:11–25.
- [31] Chen B, Bao S, Zhang Y, Li S. A high-efficiency and sustainable leaching process of vanadium from shale in sulfuric acid systems enhanced by ultrasound. Sep Purif Technol 2020;240:116624.
- [32] Li W, Ma C, Gong W, Zhu X. Clean production technology for effective recovery of vanadium from shale: interaction between activators and vanadium-loaded minerals. J Clean Prod 2021;315:128170.
- [33] Hu P, Zhang Y, Liu T, Huang J, Yuan Y. Source separation of vanadium over iron from roasted vanadium-bearing shale during acid leaching via ferric fluoride surface coating. J Clean Prod 2018;181:399–407.
- [34] Sheng M, Khan WA, Cheng S, Zhang P, Tian S, Xu Q. Characteristics of microfracturing in shales induced by dilute acid. J Nat Gas Sci Eng 2021;88:103855.
- [35] Morsy S, Hetherington CJ, Sheng JJ. Effect of low-concentration HCl on the mineralogy, physical and mechanical properties, and recovery factors of some shales. J Unconv Oil Gas Resour 2015;9:94–102.
- [36] Osiptsov AA. Fluid mechanics of hydraulic fracturing: a review. J Pet Sci Eng 2017; 156:513–35.
- [37] Carpenter C. Effect of low-concentration hydrochloric acid on properties of shale rocks. J Pet Technol 2014;66:172-6.
- [38] Tariq Z, Aljawad MS, Mahmoud M, Abdulraheem A, Al-Nakhli AR. Thermochemical acid fracturing of tight and unconventional rocks: experimental and modeling investigations. J Nat Gas Sci Eng 2020;83:103606.
- [39] Taylor R, Fyten GC, Mcneil F. Acidizing Lessons from the Past and New Opportunities. SPE-162238-MS Present. Can. Unconv. Resour. Conf., Calgary, Alberta, Canada: 2012, p. 1–13.
- [40] Rim G, Marchese AK, Stallworth P, Greenbaum SG, Park AHA. 29Si solid state MAS NMR study on leaching behaviors and chemical stability of different Mg-silicate structures for $\rm CO_2$ sequestration. Chem Eng J 2020;396:125204.
- [41] Karlsson C, Zanghellini E, Swenson J, Roling B, Bowron DT, Börjesson L. Structure of mixed alkali/alkaline-earth silicate glasses from neutron diffraction and vibrational spectroscopy. Phys Rev B - Condens Matter Mater Phys 2005;72:1–12.
- [42] Weaver CE. Clays, Muds, and Shales. New York, NY: Elsevier; 1989.
- [43] Laszlo P. Chemical reactions on clays. Science 1987;235:1473-7.
- [44] Ostrom ME. Separation of clay minerals from carbonate rocks by using acid. J Sediment Petrol 1961;31:123–9.
- [45] Asgar H, Jin J, Miller J, Kuzmenko I, Gadikota G. Contrasting thermally-induced structural and microstructural evolution of alumino-silicates with tubular and planar arrangements: case study of halloysite and kaolinite. Colloids Surfaces A Physicochem Eng Asp 2021;613:126106.
- [46] Nyam-Osor M, Soloviov DV, Kovalev YS, Zhigunov A, Rogachev AV, Ivankov OI, et al. Silver behenate and silver stearate powders for calibration of SAS instruments. J Phys Conf Ser 2012;351:012024.
- [47] Ilavsky J. Nika: software for two- dimensional data reduction. J Appl Crystallogr 2012;45:324–6.
- [48] Ilavsky J, Jemian PR. Irena: tool suite for modeling and analysis of small-angle scattering. J Appl Crystallogr 2009;42:347–53.

- [49] Beaucage G. Approximations leading to a unified exponential/power-law approach to small-angle scattering. J Appl Crystallogr 1995;28:717–28.
- [50] Fusseis F, Steeb H, Xiao X, Zhu WL, Butler IB, Elphick S, et al. A low-cost X-raytransparent experimental cell for synchrotron-based X-ray microtomography studies under geological reservoir conditions. J Synchrotron Radiat 2014;21: 251-3.
- [51] Müller CM, Pejcic B, Esteban L, Piane CD, Raven M, Mizaikoff B. Infrared attenuated total reflectance spectroscopy: an innovative strategy for analyzing mineral components in energy relevant systems. Sci Rep 2014;4:1–11.
- [52] Chen Y, Furmann A, Mastalerz M, Schimmelmann A. Quantitative analysis of shales by KBr-FTIR and micro-FTIR. Fuel 2014;116:538–49.
- [53] Yurum Y, Dror Y, Levy M. Effect of acid dissolution on the mineral matrix and organic matter of zefa oil shale. Fuel Process Technol 1985;11:71–86.
- [54] Yang X, Roonasi P, Holmgren A. A study of sodium silicate in aqueous solution and sorbed by synthetic magnetite using in situ ATR-FTIR spectroscopy. J Colloid Interface Sci 2008;328:41–7.
- [55] Harrison AL, Jew AD, Dustin MK, Thomas DL, Joe-Wong CM, Bargar JR, et al. Element release and reaction-induced porosity alteration during shale-hydraulic fracturing fluid interactions. Appl Geochem 2017;82:47–62.
- [56] Wang L, Fortner JD, Giammar DE. Impact of water chemistry on element mobilization from eagle ford shale. Environ Eng Sci 2015;32:310–20.
- [57] Wang L, Burns S, Giammar DE, Fortner JD. Element mobilization from bakken shales as a function of water chemistry. Chemosphere 2016;149:286–93.
- [58] Pilewski J, Sharma S, Agrawal V, Hakala JA, Stuckman MY. Effect of maturity and mineralogy on fluid-rock reactions in the Marcellus shale. Environ Sci Process Impacts 2019;21:845–55.
- [59] Levien L, Prewitt CT, Weidner DJ. Structure and elastic properties of quartz at pressure. Am Mineral 1980;65:920–30.
- [60] Graf DL. Crystallographic tables for the rhombohedral carbonates. Am Mineral 1961;46:1283–316.
- [61] Steinfink H, Sans FJ. Refinement of the crystal structure of dolomite. Am Mineral 1959;44:679–82.
- [62] Gruner W. The crystal structure of kaolinite. Zeitschrift Fur Krist 1932;83:75-88.
- [63] Viani A, Gualtieri A, Artioli G. The nature of disorder in montmorillonite by simulation of X-ray powder patterns. Am Mineral 2002;87:966–75.
- [64] Ramsdell LS. The crystal structures of some metallic sulfides. Am Mineral 1925;10: 281–304.

- [65] Paukert Vankeuren AN, Hakala JA, Jarvis K, Moore JE. Mineral reactions in shale gas reservoirs: barite scale formation from reusing produced water as hydraulic fracturing fluid. Environ Sci Technol 2017;51:9391–402.
- [66] Bjorlykke K, Egeberg PK. Quartz cementation in sedimentary basins. Am Assoc Pet Geol Bull 1993;77:1538–48.
- [67] McAdam AC, Zolotov MY, Mironenko MV, Sharp TG. Formation of silica by low-temperature acid alteration of Martian rocks: physical-chemical constraints. J Geophys Res E Planets 2008;113:1–8.
- [68] McLennan SM. Sedimentary silica on mars. Geology 2003;31:315-8.
- [69] Mironenko MV, Akinfiev NN, Melikhova TY. GEOCHEQ—The complex for thermodynamic modeling of geochemical systems. Vestn OGGGN RAN 2000;5: 96–7
- [70] Fitzgerald JJ, Hamza AI, Bronnimann CE, Dec SF. Studies of the Solid/Solution "Interfacial" Dealumination of Kaolinite in HCl_(aq) using solid-state 1H CRAMPS and SP/MAS 29Si NMR spectroscopy. J Am Chem Soc 1997;119:7105–13.
- [71] Matecha RM, Xiong W, Heck WF, Stewart BW, Capo RC, Hakala JA. Experimental investigation of barium sources and fluid—rock interaction in unconventional Marcellus shale wells using Ba isotopes. Energy Fuel 2022.
- [72] Renock D, Landis JD, Sharma M. Reductive weathering of black shale and release of barium during hydraulic fracturing. Appl Geochemistry 2016;65:73–86.
- [73] Singh R, Panthi K, Mohanty KK. Microencapsulation of acids by nanoparticles for acid treatment of shales. Energy Fuel 2017;31:11755–64.
- [74] Khan HJ, Spielman-sun E, Jew AD, Bargar J, Kovscek A, Druhan JL. A critical review of the physicochemical impacts of water chemistry on shale in hydraulic fracturing systems. Environ Sci Technol 2021;55:1377–94.
- [75] Beaucage G. Small-angle scattering from polymeric mass fractals of arbitrary massfractal dimension. J Appl Crystallogr 1996;29:134–46.
- [76] Voltolini M, Barnard H, Creus P, Jonathan A-F. A new mini-triaxial cell for combined high-pressure and high-temperature in-situ synchrotron X-ray microtomography experiments up to 400 °C and 24 MPa. J Synchrotron Radiat 2019;26:238-43
- [77] Object Research Systems (ORS) Inc., Dragonfly, Montreal, Canada 2020. http://www.theobjects.com/dragonfly/.
- [78] Breck DW. Zeolite molecular sieves. New York: Wiley; 1973.
- [79] Mukherjee S, Borthakur PC. Effect of leaching high sulphur subbituminous coal by potassium hydroxide and acid on removal of mineral matter and sulphur. Fuel 2003:82:783–8.